Crystal Structure at 1.8 Å Resolution and Identification of Active Site Residues of *Sulfolobus solfataricus* Peptidyl-tRNA Hydrolase

Michel Fromant, Emmanuelle Schmitt, Yves Mechulam, Christine Lazennec, Pierre Plateau,* and Sylvain Blanquet

Laboratoire de Biochimie, Unité Mixte de Recherche 7654 CNRS-Ecole Polytechnique, 91128 Palaiseau Cedex, France

Received October 27, 2004; Revised Manuscript Received January 12, 2005

ABSTRACT: The 3-D structure of the peptidyl-tRNA hydrolase from the archaea *Sulfolobus solfataricus* has been solved at 1.8 Å resolution. Homologues of this enzyme are found in archaea and eucarya. Bacteria display a different type of peptidyl-tRNA hydrolase that is also encountered in eucarya. In solution, the *S. solfataricus* hydrolase behaves as a dimer. In agreement, the crystalline structure of this enzyme indicates the formation of a dimer. Each protomer is made of a mixed five-stranded β-sheet surrounded by two groups of two α-helices. The dimer interface is mainly formed by van der Waals interactions between hydrophobic residues belonging to the two N-terminal α1 helices contributed by two protomers. Site-directed mutagenesis experiments were designed for probing the basis of specificity of the archaeal hydrolase. Among the strictly conserved residues within the archaeal/eucaryal peptidyl-tRNA hydrolase family, three residues, K18, D86, and T90, appear of utmost importance for activity. They are located in the N-part of α1 and in the β3−β4 loop. K18 and D86, which form a salt bridge, might play a role in the catalysis thanks to their acid and basic functions, whereas the OH group of T90 could act as a nucleophile. These observations clearly distinguish the active site of the archaeal/eucaryal hydrolases from that of the bacterial/eucaryal ones, where a histidine is believed to serve as the catalytic base.

During elongation of a new polypeptide, peptidyl-tRNAs can dissociate prematurely from the ribosome. As a result, peptidyl-tRNAs are produced in the cell. Such peptidyl-tRNAs cannot be consumed by the translation machinery. To reuse the sequestered tRNAs, cells display peptidyl-tRNA hydrolase activities carried by specific enzymes. In bacteria, the peptidyl-tRNA hydrolase (Pth1) serves an essential function for cell viability (*1*−*4*). Because of this, bacterial Pth1s are attractive targets for antimicrobial agents (*5*, *6*). In archaea, another type of peptidyl-tRNA hydrolase (Pth2) has been found (*7*, *8*). It is shorter in length and lacks any obvious homology to Pth1. Interestingly, all available eucaryal genomes show at least one archaeal-like pth2 gene, while most of them also display one or several bacterial-like pth1 gene(s). For instance, the *Arabidopsis thaliana* genome indicates four bacterial-like Pth1s and three archaeal-like Pth2s. Finally, as we shall see later in the present study, a Pth2-like domain can be distinguished in one member of the proteome of several actinomycetales (Figure 1). In the predicted protein, the Pth2 domain is linked to an N-terminal domain specific to these organisms. The function of the whole protein is unknown. Surprisingly, a Pth2-like domain can also be detected in one protein encoded by the fowlpox or canarypox virus genomes.

The crystal structure of monomeric *Escherichia coli* Pth1 (193 residues) has been solved at 1.2 Å resolution (*4*). It is formed of a single α/β globular domain built around a twisted mixed β-sheet similar to the central core of an aminopeptidase from *Aeromonas proteolytica*. Three residues, N10, H20, and D93, are crucially involved in the enzyme activity. Recent work indicates that H20 might act as the catalytic base in the mechanism of bacterial Pth1 (*6*).

Recently, the crystal structure of a C-portion (116 residues) of a *Homo sapiens* Pth2 (huPth2)[1] was solved at 2.0 Å resolution (*9*). This truncated protein is derived from a polypeptide also called Bcl-2 inhibitor of transcription 1 [Bit1 (*10*)]. It carries peptidyl-tRNA hydrolase activity and is described to behave as a monomer. It shows an α/β fold with a four-stranded antiparallel β-sheet in its core, surrounded by two α-helices on each side. From the observation of this structure, several residues belonging to the β1−α1 and the β3−β4 loops were proposed as candidates for forming the active site of the enzyme.

In this study, the 3-D structure of peptidyl-tRNA hydrolase from the archaea *Sulfolobus solfataricus* (suPth2) is described at 1.8 Å resolution. This protein contains 120 residues. The folding is similar to that of *H. sapiens* Pth2. However, there is a marked deviation at the level of the β3−β4 loop conformation. Another difference between the two proteins relates to the dimeric character of suPth2 in solution. In agreement, two dimers could be identified in the asymmetric unit of suPth2 crystals, with a dimer interface formed by van der Waals contacts between hydrophobic residues belonging to the α1 helices contributed by each protomer. Notably, a similar arrangement can be recognized within the crystals of huPth2, thereby suggesting the possible significance of huPth2 dimer formation in the biological function

* To whom correspondence should be addressed. Fax: +33 1 69 33 30 13. Tel: +33 1 69 33 41 81. E-mail: plateau@bioc.polytechnique.fr.

[1] Abbreviations: PTH, peptidyl-tRNA hydrolase; suPth2, *Sulfolobus solfataricus* peptidyl-tRNA hydrolase; huPth2, *Homo sapiens* peptidyl-tRNA hydrolase; NCS, noncrystallographic symmetry; IPTG, isopropyl β-D-thiogalactopyranoside; PMSF, phenylmethanesulfonyl fluoride.

10.1021/bi047711k CCC: $30.25
Published on Web 02/17/2005

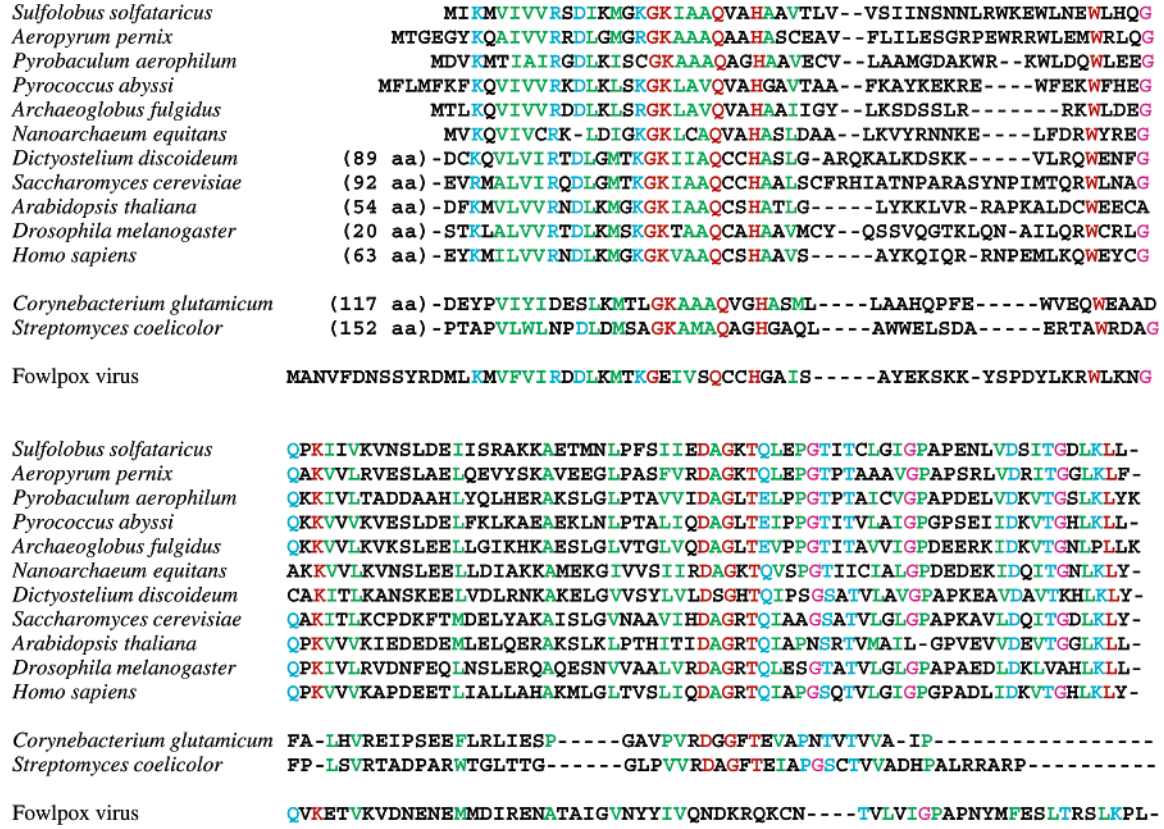

FIGURE 1: Sequence alignment of pth2 gene products from representative archaeal and eucaryal species. Two sequences of Pth2 orthologues found in actinomycetales are also shown. Finally, the sequence of the orthologue of fowlpox virus is represented. Residues are colored according to their conservation status, taking into account the 46 Pth sequences available in the Swiss-Prot and TrEMBL databases. Pth2 sequences from actinomycetales and from fowlpox virus were excluded from the definition of the pattern. Strictly conserved positions among the 46 Pth2 sequences are in red. Other highly conserved positions (in more than in 85% of the compared sequences) are highlighted with the following color code: green for hydrophobic residues (V, I, L, M, W, F, A, P), pink for glycine, blue for R or K, Q or E, D or N, and T or S.

of this protein. Finally, site-directed mutagenesis experiments were designed at probing the basis of specificity of the archaeal Pth2. Among the strictly conserved residues within the Pth2 family, three residues, K18, D86, and T90, appear of utmost importance for activity. They are in the N-part of α1 and in the $\beta3-\beta4$ loop. K18 and D86, which form a salt bridge, might play functions of acid and base catalysts in the esterase reaction whereas T90 could act as a nucleophile.

MATERIALS AND METHODS

Crystallization and Data Collection. suPth2 was purified as described elsewhere (*8*). Screening for crystallization conditions was performed at 24 °C by the vapor diffusion method in hanging drops, using Crystal Screen I and II sparse matrix solutions [Hampton Research (*11*)]. The drops were prepared by mixing 2.7 μL of protein (1.3 mg/mL in 20 mM Tris-HCl, pH 7.0, 0.1 mM EDTA, and 10 mM 2-mercaptoethanol) with 0.7 μL of $tRNA_f^{Met}$ (11 mg/mL) and 2 μL of reservoir solution. Crystals devoid of tRNA were obtained within a few days in condition 49 of Crystal Screen I (0.8 M $LiSO_4$, 1.6% PEG 8000). When used, the pH of this unbuffered solution was measured equal to 2.8. Cryoprotection conditions for recording at 100 K were defined as 0.64 M $LiSO_4$ (pH adjusted at 2.8 with H_2SO_4), 1.28% PEG 8000, and 20% glycerol. Using synchrotron radiation (ESRF, Grenoble, France; ID14-EH4 beamline; $\lambda = 1.0$ Å), cryocooled crystals diffracted to 1.8 Å resolution. Crystals of suPth2 belong to space group $P2_1$ with cell parameters $a =$ 46.8 Å, $b = 67.2$ Å, $c = 85.4$ Å, and $\beta = 95.1°$. Data were processed using Mosflm (*12*) and programs of the CCP4 package (*13*) (Table 1).

Phase Determination and Model Building. A single isomorphous heavy atom derivative could be obtained by soaking the native crystals during 24 h at 24 °C in a solution containing 0.8 M $LiSO_4$, 1.6% PEG 8000, and 1 mM mercuric bromide. With this derivative, diffraction data were collected at the ID14-EH3 beamline (ESRF, Grenoble, France) using X-rays at a wavelength of 0.931 Å. The native and derivative datasets were then input to the program SOLVE (*14*). Four mercury sites were found and refined. After solvent flattening using RESOLVE (*15*), a map was calculated with data up to 3 Å resolution. The quality of the obtained map was sufficient to identify some secondary structure elements in each of the four protomers composing the asymmetric unit. This allowed the definition of a noncrystallographic symmetry (NCS) mask as well as that of the NCS operators. Four-fold NCS averaging and solvent flattening with DM (*16*) improved the quality of the phases. The size of the mask was then gradually increased to cover most of a protomer.

The quality of the NCS-averaged map was such that most of the backbone of one polypeptide could be readily constructed using O (*17*). After a few rounds of refinement using CNS (*18*) with NCS restraints, refinement was continued without NCS restraints. The final *R* factor was 20.5% and free *R* was 22.4% (with 6% of the data left out

Table 1: Native and Heavy Atom Derivative Data Used in Structure Determination of *S. solfataricus* Peptidyl-tRNA Hydrolase[a]

	native	$HgBr_2$
data collection		
reagent concn (mM)		1
soaking time (h)		24
X-ray source	ESRF ID14-EH4	ESRF ID14-EH3
wavelength (Å)	1.0	0.931
processing	Mosflm	Mosflm
resolution (Å)	1.80	3.0
completeness	99.9 (99.9)	98 (96.2)
redundancy	5.4	6.6
$R_{sym}(I)$ (%)	6.5 (11.2)	10.9 (32.4)
figure of merit before density modification		0.35
refinement statistics		
resolution range (Å)	500−1.8	
unique reflections (free)	45563 (2925)	
R_{work} (%)	20.5	
R_{free} (%)	22.4	
no. of residues	120 × 4	
no. of water molecules	498	
no. of sulfate ions	8	
rmsd, bond lengths (Å)	0.0050	
rmsd, angles (deg)	1.12	
mean *B* values		
mono 1	23.3	
mono 2	18.4	
mono 3	22.5	
mono 4	17.6	
sulfate	53.0	
water	37.5	
NCS deviations (Å)		
mono 2	0.24	
mono 3	0.16	
mono 4	0.23	

[a] Space group $P2_1$; cell dimensions, $a = 46.8$ Å, $b = 67.2$ Å, $c = 85.4$ Å, and $\beta = 95.1°$.

of the calculations). The obtained model shows very good geometry with rms deviations from ideal geometry of 0.0050 Å for bond lengths and of 1.12 deg for bond angles. All residues lie within the allowed regions of the Ramachandran plot. The final density was of very good quality for the four protomers. The loop linking β3 to β4 (from residue 89 to residue 91) was less ordered in protomers 1, 2, and 4 than in protomer 3.

Coordinates have been deposited in the PDB with the accession number 1XTY.

Production and Purification of Enzyme Mutants. The *S. solfataricus* pth2 gene was amplified by PCR using plamsid pTrc-pthS (*6*) as template and oligonucleotides GGGAATTCCATATGATTAAGATG and CGCGGATCCTCACAGTAATTTT. The resulting DNA fragment was digested by both *Nde*I and *Bam*HI and inserted into the corresponding sites of plasmid pET3a (Novagen) to give plasmid pETpthSS. For site-directed mutagenesis, pETpthSS containing the desired mutation was synthesized by DNA polymerization using a pair of complementary mutagenic primers and PfuTurbo DNA polymerase (Stratagene). After thermal cycling, methylated wild-type DNA was restricted in the presence of *Dpn*I before transformation of XL1-Blue cells. Entire sequences of the mutated pth2 genes were systematically verified.

E. coli Rosetta (Invitrogen) was transformed by the pETpthSS plasmid carrying the *S. solfataricus* PTH gene with the desired mutation. Transformed cells were grown at 37 °C in 0.5 L of 2×TY medium containing 50 μg/mL ampicillin. When the value of the optical density at 650 nm reached 2, IPTG was added at a final concentration of 1 mM, and growth was continued for 7 h at room temperature. Cells were harvested by centrifugation for 30 min at 4000*g*. From this step on, all buffers used for the purification of peptidyl-tRNA hydrolase systematically contained 10 mM 2-mercaptoethanol and 0.1 mM EDTA. The cell pellet was suspended in 12 mL of 50 mM Tris-HCl (pH 7.0) containing 0.1 mM PMSF. Cells were disrupted by sonication (10 min, 0 °C), and debris was removed by centrifugation (10 min, 20000*g*). The resulting supernatant was heated at 80 °C for 10 min and centrifuged at 20000*g* for 10 min. The obtained supernatant was applied onto a Superdex 75 column (320 mL, 2.6 × 60 cm, from Amersham Biosciences) equilibrated in 20 mM Tris-HCl (pH 7.0) containing 500 mM KCl. Elution was performed at a flow rate of 1.4 mL/min. Active fractions were pooled and applied on a hydroxylapatite column (1.1 × 10 cm) equilibrated in 5 mM potassium phosphate (pH 7.0). Elution was carried out at a flow rate of 0.2 mL/min using a 200 mL linear gradient of 5−600 mM potassium phosphate (pH 7.0). PTH activity free of contaminating nucleic acids was recovered at 400 mM potassium phosphate. After dialysis against 20 mM potassium phosphate (pH 7.0), the protein sample was chromatographed on an SP-Sepharose column (1 × 2 cm) equilibrated in the same buffer. Elution was performed using a linear gradient from 0 to 500 mM KCl in the buffer of the column (0.25 mL/min, 500 mM/h). Fractions exhibiting activity were pooled and finally dialyzed against 20 mM Tris-HCl buffer (pH 7.0) containing 0.1 mM EDTA, 0.1 mM dithiothreitol, 400 mM KCl, and 60% glycerol. Recovered enzyme solution was stored at −20 °C.

All mutants were at least 95% homogeneous according to SDS−PAGE analysis. Migration of the K118A PTH variant was slightly slower than that of the wild-type enzymes or of the other mutant PTHs. The molecular mass of the K118A protein was verified by nano ESI mass spectrometry using a 7 T FTICR mass spectrometer APEX III (Bruker Daltonics, Billerica, MA). Molecular masses of 13082 and 13139 Da were obtained for the K118A species and the wild-type protein, respectively. These two values exactly correspond to the masses expected from the sequences of the two compared species. Therefore, we concluded that the particular migration of the mutant K118A PTH could not be accounted for by abnormal transcription of the mutant gene nor by posttranslational modification of the mutant protein.

Concentrations of purified PTHs were determined using a molecular ratio (~2 × 13100) and a light absorption coefficient (1.269 A_{280} units·mg^{-1}·mL) calculated from the amino acid sequence of the protein.

Assay of Peptidyl-tRNA Hydrolase Activity. E. coli $tRNA^{Lys}$ was produced, aminoacylated with L-[^{3}H]lysine (3.1, 335.6, or 36000 Ci/mol), N-acetylated, and purified on Chelex 100 and Trisacryl GF05 as described previously (*4*). Unless otherwise stated, measurements of *S. solfataricus* PTH activity were performed at 50 °C for 5 min in 100 μL assays containing 20 mM Tris-HCl (pH 7.5), 10 mM $MgCl_2$, 0.1 mM EDTA, 0.1 mM dithiothreitol, 0.2 mg/mL herring sperm DNA, 0.15−200 nM diacetyl[^{3}H]lysyl-$tRNA^{Lys}$, and limiting amounts of enzyme to give initial rate measurements: 5−100

pM (wild-type suPth2 and Q54A and K118A mutants), 0.02−2 nM (Q22A, H25A, K56A, and T98A), 0.5−2 nM (T90A), or 2−4 nM (K18A, D86A, and K18A/D86A). Addition of DNA in the reaction mixture was made in order to avoid adsorption of the radioactive substrate on the microtube walls. As shown before (*8*), *S. solfataricus* PTH activity is insensitive to the addition of DNA in the assay mixture. The reaction was quenched by the addition of 340 μL of ethanol, 14 μL of sodium acetate (3 M, pH 4.8), and 20 μL of carrier RNA from yeast (4 mg/mL). Samples were then centrifuged. Soluble radioactivity in the recovered supernatant was measured by scintillation counting, as described (*8*). Data were systematically corrected for spontaneous hydrolysis of the substrate in the absence of PTH.

K_m and k_{cat} values were derived from iterative nonlinear fits of the theoretical Michaelis equation to the experimental values using the Levenberg−Marquardt algorithm. Confidence limits on the fitted values were obtained by 100 Monte Carlo simulations followed by least-squares fitting using the experimental standard deviations on individual measurements (*19*).

RESULTS AND DISCUSSION

Overall Structure of S. solfataricus Peptidyl-tRNA Hydrolase. The structure of *S. solfataricus* peptidyl-tRNA hydrolase was solved by using data from an isomorphous derivative including anomalous scattering information (λ = 0.931 Å; SIRAS). Phasing was then improved by solvent flattening and 4-fold noncrystallographic symmetry averaging. The asymmetric unit contains four protomers. The final model refined at 1.8 Å resolution contains all of the 4 × 120 amino acid residues, as well as 498 water molecules and 8 sulfate ions.

We have established by molecular sieving that suPth2 behaves in solution as a dimer (*8*). In agreement with this conclusion, two dimers could be easily identified in the asymmetric unit. The corresponding protomers, termed proto 1 and proto 2 (dimer 1) and proto 3 and proto 4 (dimer 2), respectively, display extensive contacts. The accessible surface of a protomer is 6620 Å^2 with a surface of 1800 Å^2 buried in the dimer interface. Another 2-fold NCS axis relates the two dimers in the asymmetric unit.

Each protomer is made of a mixed β-sheet (five strands) surrounded by two groups of two α-helices (Figure 2B,C). The dimer interface involves α1 helix (residues 16−35), residues 50−55, and the N-terminal end of the β2 strand (residues 56−58). In protomer 1, the N-terminal part of α1 is wedged between α1 and β2 of protomer 2 (Figure 2C). Most of the corresponding contacts are through van der Waals interactions between hydrophobic residues of α1. The two α1 helices belonging to protomers 1 and 2 are parallel and pack one to each other in such a way that one residue in the first α1 helix interacts with the corresponding residue in the second α1 helix. Involved side chains are those of K16, A20, A24, A27, V28, V31, and I35. Hence, the dimer interface at the N-terminus of the two α1 helices is capped by the two K16 residues belonging to protomers 1 and 2. The two lysine residues interact together through the aliphatic part of their side chains. In addition, the side chains of T29 of one protomer and of Q54 of the other associated protomer are hydrogen bonded.

The 3-D structure of huPth2 has been recently solved (*9*). It can be superimposed on that of suPth2 (protomer 3) with an rms value of 1.1 Å for 111 C-α atoms compared. On examination of the crystalline form of huPth2, a dimer can be drawn which exactly fits in with the dimer of suPth2 (with dimer 2, the rms deviation is 1.2 Å for 222 C-α atoms compared). Such a coincidence of dimers in two different crystalline systems argues in favor of the possible significance of huPth2 dimer formation in the accomplishment of the biological function of this protein. The 3-D models of two other proteins showing similarity to Pth2 have been recently deposited at the PDB. The first one, a *Thermoplasma acidophilum* protein (PDB 1RLK), has a crystal structure superimposable to that of suPth2, with an rms value of 0.88 Å for 110 C-α atoms. A dimer identical to that displayed by suPth2 can be recognized in the crystal, the second protomer of the dimer being generated by a crystallographic operator of symmetry. The structure of the second protein, from *Archaeoglobus fulgidus*, was solved in solution by NMR (PDB 1RZW). It shows a fold similar to that of suPth2, with an rms of 2 Å for 65 compared C-α atoms.

Identification of Residues Involved in Activity. Alignment of the available sequences of Pth2 from various eukaryotic and archaeal sources allowed us to highlight strongly conserved residues (Figures 1 and 2A). One of them, W49, is buried inside the protein, indicating a possible role in the folding of each protomer. K16 and Q54 are located at the interface between the two protomers. These residues are likely to participate in dimer formation (see above). Several residues (K18, Q22, H25, K56, D86, T90, Q91, P94, T96, and T98) are clustered in a region encompassing the N-terminal part of helix α1, the β3−β4 loop of one protomer and β2 and β5 of the second protomer (Figures 2 and 3). To assess a possible role of this cluster in PTH activity, residues K18, Q22, H25, K56, D86, T90, and T98 were each mutated to alanine. With each purified mutant protein, catalytic parameters were measured using *E. coli* diacetyllysyl-tRNA^{Lys} as substrate (Table 2). All studied residues appear to be of importance for activity. In particular, mutations of K18 or D86 reduce the catalytic efficiency (k_{cat}) by 4 orders of magnitude, whereas modification of T90 reduces the k_{cat} value by 2 orders of magnitude. On the other hand, K_m variations associated with these three mutations are small, therefore indicating that the three studied residues do not much interfere with the preequilibrium between the enzyme and its substrate.

In the crystal, K18 and D86 interact through a salt bridge between their side chains. Interestingly, the double mutant (D86A/K18A) keeps the same activity as either of the two point mutants (D86A or K18A, Table 2). T90 belongs to a mobile loop joining β3 to β4. It overhangs K18 and D86 in such a way that the side chain of T90 lies at proximity of K18 (3.70 Å). Below K18, D86, and T90, the Q22 and T98 residues form a second layer. These two residues are held together by a hydrogen bond between their side chains. They appear to be involved in catalysis since, upon modification of the one or the other, k_{cat} is reduced by a factor of 30-fold if compared to the native enzyme. In the dimer structure, the side chain of H25 of one protomer and the side chain of K56 of the second protomer form a third, more buried, layer of residues. Kinetic parameters (k_{cat}) of mutants K56A and H25A are lowered by factors of 25 and 16, respectively. Such

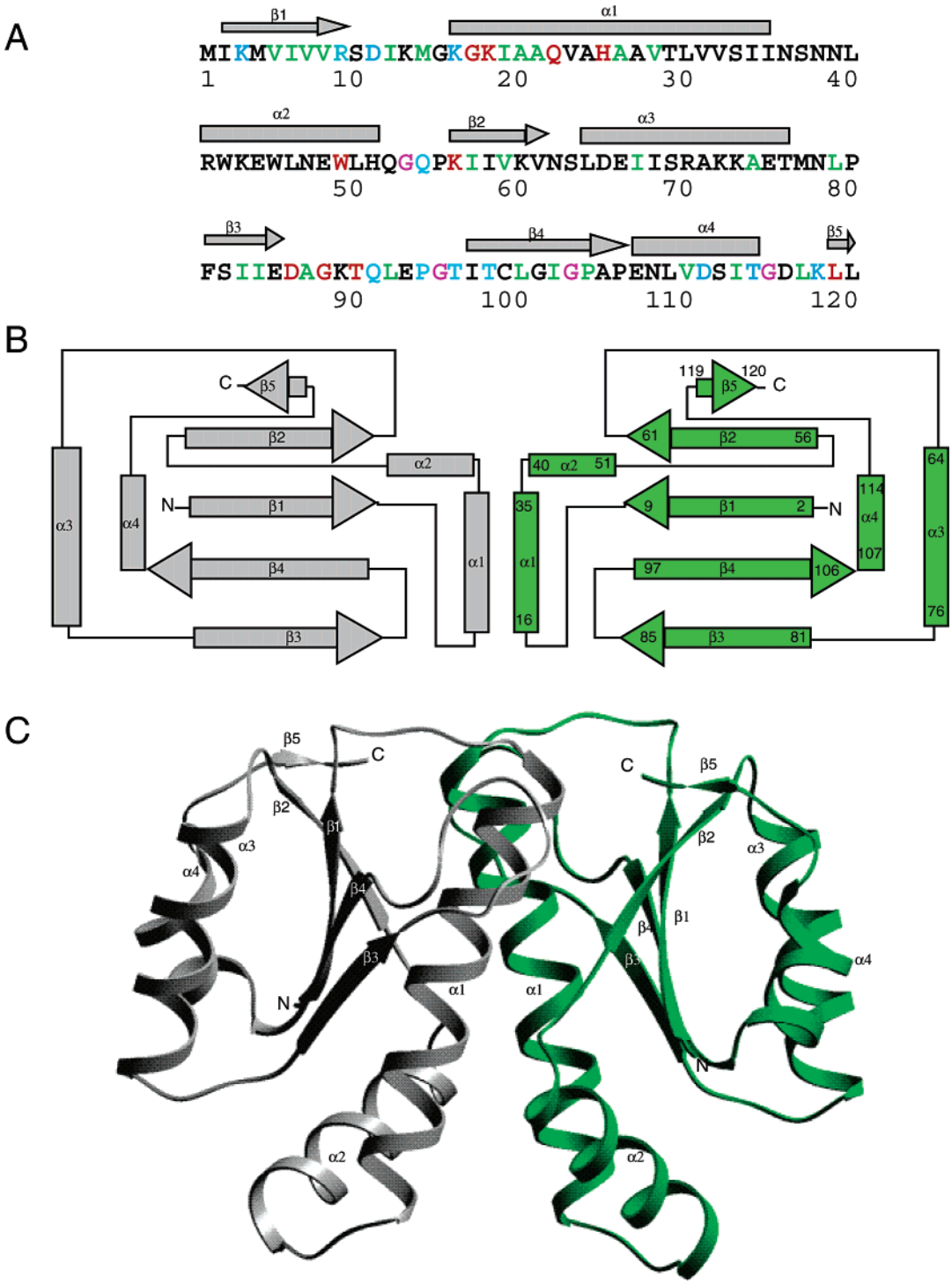

FIGURE 2: (A) Sequence of suPth2 showing the pattern of conserved residues as described in Figure 1. Secondary structure elements were assigned by using the Yasspa program implemented in O (*17*). The elements are drawn above the sequence. Strands are represented by arrows and helices by rods. (B) Topology of the suPth2 dimer. The numbering refers to the residues delineating each structural element. One protomer is colored in green and the other protomer in gray. (C) Schematic drawing of dimeric suPth2. The coloring is the same as that used in panel B of this figure. Secondary structure elements are labeled as defined in panels A and B of this figure. The figure was drawn with Setor (*20*).

decreases indicate contribution of these two residues to catalysis.

Q54 of one protomer interacts with T29 of the second protomer. To assess the importance of Q54 in the dimerization process, a Q54A mutant was produced. In solution, at a concentration of 1.5 μM, this mutant still behaves as a dimer, as shown by HPLC molecular sieving (*8*). Therefore, other van der Waals contacts must be considered to account for the stability of the dimeric structure. On the other hand, introduction of the Q54A mutation reduces the k_{cat} value by a factor of 6. Possibly, the proximity of the Q54 side chain to that of H25 (3.5 Å) accounts for such an effect.

The above results establish a link between the activity of suPth2 and the cluster of residues encompassing the N-terminal part of helix α1, the $\beta3-\beta4$ loop of one protomer and $\beta2$ and $\beta5$ of the second protomer. By assuming that

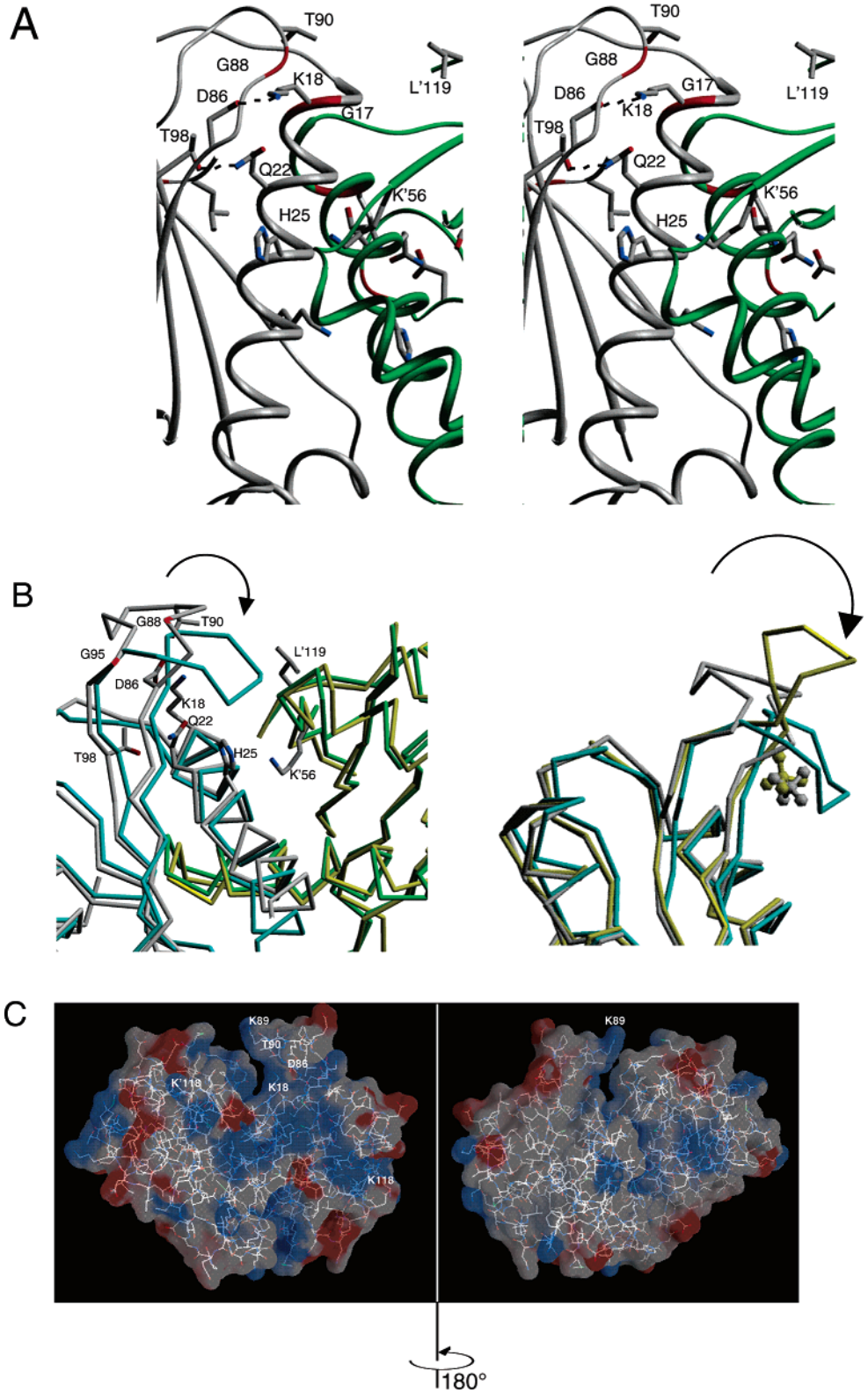

FIGURE 3: (A) Stereoview of the putative active site of dimeric suPth2. Locations of the strictly conserved residues delineating the catalytic pocket are shown. One protomer is colored in green and the other one in gray. Hydrogen bonds between K18 and D86 and between Q22 and T98 are shown by dashed lines. Residues belonging to the second protomer are flagged by a prime. (B) Left: Superimposition of the 3-D models of suPth2 and huPth2 (*9*). Protomers of suPth2 are colored in gray and green. Putative residues in the active site of suPth2 are shown and labeled. Protomers of huPth2 are colored in blue and yellow. An arrow highlights the different positions of the $\beta3-\beta4$ loop in suPth2 and in huPth2. Mobility of the polypeptide chain in this region may arise from the hinge resulting from G88 and G95. Right: Comparison of the conformations of the $\beta3-\beta4$ loops in the Pth2 from *S. solfataricus* (gray, PDB 1XTY), human (blue, PDB 1Q7S), and *T. acidophilum* (yellow, PDB 1RLK). The sulfate ions present in the active site cavities of the *S. solfataricus* and *T. acidophilum* enzymes are drawn in gray and yellow, respectively. The $\beta3-\beta4$ loop of the *A. fulgidus* protein also presents a different conformation but was not represented for the sake of clarity. (C) Molecular surfaces of the protein showing the electrostatic potential calculated with the Delphi program (*21*) and rendered with Grasp (*22*). The two views differ by a rotation of 180° around the vertical axis. Negatively charged regions are colored in red and positively charged ones in blue. Positions of T90, D86, and K18 delineating the putative catalytic center are indicated as well as those of K89 (loop $\beta2-\beta3$), K118 (protomer 1), and K′118 (protomer 2).

Table 2: Catalytic Parameters of the Various Studied PTH Variants[a]

enzyme	k_{cat} (s^{-1})	K_m (nM)	relative k_{cat}/K_m
WT	1.8 ± 0.2	9.1 ± 1.6	100
K18A	0.0020 ± 0.0005	5.3 ± 1.5	0.2
Q22A	0.06 ± 0.015	1.6 ± 0.8	20
H25A	0.10 ± 0.02	4.4 ± 0.7	13
Q54A	0.27 ± 0.02	2.9 ± 0.3	47
K56A	0.07 ± 0.01	3.2 ± 0.6	12
D86A	0.0025 ± 0.0005	5.4 ± 0.8	0.22
T90A	0.02 ± 0.01	7.2 ± 1.6	1.4
T98A	0.06 ± 0.01	0.9 ± 0.4	34
K118A	2.2 ± 0.2	12.8 ± 1.8	87
D86A/K18A	0.0020 ± 0.0005	6.7 ± 1.8	0.17

[a] Michaelian k_{cat} and K_m parameters were measured as described in Materials and Methods. Relative k_{cat}/K_m values were given an arbitrary value of 100 to the measurement with wild-type enzyme.

this cluster corresponds to one catalytic site, two active sites should be present in a dimer. In each such site, K18 and D86, which form a salt bridge, might play a role in the catalysis thanks to their acid and basic functions, whereas the OH group of T90 could act as a nucleophile. Concerted action of K18 and D86 in the cleavage of the ester bond in an N-blocked aminoacyl-tRNA is argued for by the observation that the double mutation (D86A/K18A) does not affect the catalytic rate more than each of the corresponding single mutations. One likely explanation is that D86 lowers the pK_a value of K18, therefore reinforcing the reactivity of the lysine in the attack the carbonyl group in the ester bond.

Notably, in the crystallized protein, a sulfate ion is tightly bound inside the putative active site crevice, very close to the putative catalytic center. This ion is held by the side chains of Q22, D86 (via a water molecule), K18 (via two water molecules), K56 (via two water molecules), and the main chain NH group of A87. Interestingly, in the structure of the *T. acidophilum* protein (PDB 1RLK), a sulfate ion is present at the same position (rmsd 0.5 Å). Possibly, this sulfate mimics one phosphate of the CCA end of the tRNA substrate. It also shows easy access of solute molecules to the enzyme center.

In the suPth2 density map, protomer 3 shows an unambiguous conformation of its $\beta3-\beta4$ loop. In contrast, the loops in the three other protomers appear more mobile, although they keep a constant overall conformation. Upon superimposition of suPth2 on huPth2 or on *T. acidophilum* Pth2, strong deviations of the $\beta3-\beta4$ loop conformations are observed (Figure 3B), with a flipping motion around the hinge formed by G88 and G95. G88 is a strictly conserved residue in the Pth2 family, while G95 is replaced by N in 17% of the compared Pth2 sequences. These observations suggest that flexibility of the $\beta3-\beta4$ loop region may be important for catalysis and that this property was retained by evolution in all Pth2 structures by keeping a glycine at position 88. In a neighboring loop between $\beta1$ and $\alpha1$, a 9-RXD-11 motif is well conserved. Superimposition of the three crystal structures indicates a constant conformation for this region. Notably, the arginine residue is clamped by both the aspartate residue and the carbonyl group of the N-terminal residue of $\beta4$. Such contacts could contribute to productive binding of the acceptor end of tRNA inside the active site.

In the case of Pth1, the tRNA substrate is predicted to be held at the surface of the protein through the clamping of its 5′-phosphoryl end by two basic residues (*4*). In contrast to Pth1, Pth2 activity is poorly sensitive to the presence or the absence of a 5′-phosphoryl group at the top of the tRNA substrate (*8*). In agreement with this observation, we could not detect any strictly conserved basic residue at the surface of Pth2. An electrostatic potential representation of the structure in Figure 3C shows, however, a concentration of cationic residues on one side of the molecule, in the vicinity of the putative active site. This region may correspond to a potential surface for tRNA recognition. Within this region, a lysine, K118, is conserved in 42 out of the 46 Pth2 sequences used in our alignment (Figure 2). Moreover, this lysine, on one protomer, is presented in the vicinity of the active site cleft on the other protomer. We searched for a possible role of K118 in the activity of the enzyme. However, as shown in Table 2, mutation of K118 into A does not significantly change the catalytic parameters. A major role of K118 in the mechanism of action of Pth2 can be therefore disfavored.

Figure 1 compares the sequences of several archaeal and eucaryal Pth2s to those of two proteins from actinomycetales having a Pth2-like domain. The performed alignments indicate that, with the exception of K56 and K118, all of the residues discussed above are conserved in the Pth2-like domains. This coincidence strongly suggests that the Pth2 orthologues found in actinomycetales possess an esterase activity resembling that of a Pth2. In the case of the fowlpox virus, although the Pth2 orthologue is likely to adopt a fold similar to that of a typical Pth2, the active site residues characteristic of Pth2 are absent, suggesting a yet unknown function for this orthologue.

CONCLUDING REMARKS

Pth1 and Pth2 are different at the level of their amino acid sequences and 3-D folds. This study indicates distinct chemical compositions of the active clefts for the two families of enzymes. Such a conclusion reinforces the view that bacterial Pth1 represents an attractive target for antimicrobial agents (*5*, *6*). Indeed, even if such agents were dangerous for the activity of the products of eukaryotic pth1-like gene(s), the pth2-like gene product(s) should resist and help the eukaryotic host to survive. In fact, the growth of a eukaryote, *Saccharomyces cerevisiae*, has been reported to be unaffected by inactivation of both its pth1- and pth2-like genes, which suggests that this cell should be insensitive to any chemical agent specific for Pth1 (*7*, *8*). One likely explanation is that a third type of Pth activity occurs in yeast and, possibly, in all eukaryotes. Identification of such a new peptidyl-tRNA hydrolase clearly deserves attention.

ACKNOWLEDGMENT

We thank J. Mc Carthy and the staff of ESRF for helpful advice during data collection on id14eh3 and id14eh1. We are grateful to M. L. Ferri-Fioni for the construction of plasmid pETpthSS, G. van der Rest for performing the mass spectrometry analysis, and M. Vanoni for early contribution to this work.

REFERENCES

1. Atherly, A. G., and Menninger, J. R. (1972) Mutant *E.coli* strain with temperature sensitive peptidyl-transfer RNA hydrolase, *Nat. New Biol. 240*, 245−246.

2. Garcia-Villegas, M. R., De La Vega, F. M., Galindo, J. M., Segura, M., Buckingham, R. H., and Guarneros, G. (1991) Peptidyl-tRNA hydrolase is involved in λ inhibition of host protein synthesis, *EMBO J. 10*, 3549−3555.
3. Menninger, J. R., and Coleman, R. A. (1993) Lincosamide antibiotics stimulate dissociation of peptidyl-tRNA from ribosomes, *Antimicrob. Agents Chemother. 37*, 2027−2029.
4. Schmitt, E., Mechulam, Y., Fromant, M., Plateau, P., and Blanquet, S. (1997) Crystal structure at 1.2 Å resolution and active site mapping of *Escherichia coli* peptidyl-tRNA hydrolase, *EMBO J. 16*, 4760−4769.
5. Bonin, P. D., Choi, G. H., Trepod, C. M., Mott, J. E., Lyle, S. B., Cialdella, J. I., Sarver, R. W., Marshall, V. P., and Erickson, L. A. (2002) Expression, purification and characterization of peptidyl-tRNA hydrolase from *Staphylococcus aureus*, *Protein Expression Purif. 24*, 123−130.
6. Goodall, J. J., Chen, G. J., and Page, M. G. (2004) Essential role of histidine 20 in the catalytic mechanism of *Escherichia coli* peptidyl-tRNA hydrolase, *Biochemistry 43*, 4583−4591.
7. Rosas-Sandoval, G., Ambrogelly, A., Rinehart, J., Wei, D., Cruz-Vera, L. R., Graham, D. E., Stetter, K. O., Guarneros, G., and Söll, D. (2002) Orthologs of a novel archaeal and of the bacterial peptidyl-tRNA hydrolase are nonessential in yeast, *Proc. Natl. Acad. Sci. U.S.A. 99*, 16707−16712.
8. Fromant, M., Ferri-Fioni, M. L., Plateau, P., and Blanquet, S. (2003) Peptidyl-tRNA hydrolase from *Sulfolobus solfataricus*, *Nucleic Acids Res. 31*, 3227−3235.
9. De Pereda, J. M., Waas, W. F., Jan, Y., Ruoslahti, E., Schimmel, P., and Pascual, J. (2004) Crystal structure of a human peptidyl-tRNA hydrolase reveals a new fold and suggests basis for a bifunctional activity, *J. Biol. Chem. 279*, 8111−8115.
10. Jan, Y., Matter, M., Pai, J. T., Chen, Y. L., Pilch, J., Komatsu, M., Ong, E., Fukuda, M., and Ruoslahti, E. (2004) A mitochondrial protein, Bit1, mediates apoptosis regulated by integrins and Groucho/TLE corepressors, *Cell 116*, 751−762.
11. Jancarik, J., and Kim, S. H. (1991) Sparse matrix sampling: a screening method for crystallization of proteins, *J. Appl. Crystallogr. 24*, 409−411.
12. Leslie, A. (1990) *Crystallographic computing V*, Oxford University Press, Oxford, U.K.
13. Collaborative Computational Project No. 4 (1994) The CCP4 suite: programs from protein crystallography, *Acta Crystallogr. D50*, 760−763.
14. Terwilliger, T. C., and Berendzen, J. (1999) Automated MAD and MIR structure solution, *Acta Crystallogr., Sect. D: Biol. Crystallogr. 55* (Part 4), 849−861.
15. Terwilliger, T. C. (2003) SOLVE and RESOLVE: automated structure solution and density modification, *Methods Enzymol. 374*, 22−37.
16. Cowtan, K. (1994) *Jt. CCP4 and ESF-EACBM Newsl. Protein Crystollagr. 31*, 34−38.
17. Jones, T. A., Zou, J. Y., Cowan, S. W., and Kjeldgaard, M. (1991) Improved methods for the building of proteins model in electron density maps and the location of errors in these models, *Acta Cystallogr. A47*, 110−119.
18. Adams, P. D., Pannu, N. S., Read, R. J., and Brunger, A. T. (1997) Cross-validated maximum likelihood enhances crystallographic simulated annealing refinement, *Proc. Natl. Acad. Sci. U.S.A. 94*, 5018−5023.
19. Dardel, F. (1994) MC-Fit: Using Monte-Carlo methods to get accurate confidence limits on enzyme parameters, *Comput. Appl. Biosci. 10*, 273−275.
20. Evans, S. V. (1993) Setor: hardware lighted three-dimensional solid model representation of macromolecules, *J. Mol. Graphics 11*, 134−138.
21. Nicholls, A., and Honig, B. (1991) A rapid finite difference algorithm utilizing successive over-relaxation to solve the Poisson-Boltzmann equation, *J. Comput. Chem. 12*, 435−445.
22. Nicholls, A., Sharp, K. A., and Honig, B. (1991) Protein folding and association: insights from the interfacial and thermodynamic properties of hydrocarbons, *Proteins 11*, 281−286.

BI047711K